

# Power Quality Improvement in Hybrid E-Bicycles Using the Adaptive Reinforcement Current Tracking-based Super-Lift Converter

Shajini G Inba Kani<sup>1</sup>, P. Elangovan<sup>1,\*</sup>

<sup>1</sup>Department of EEE, B.S.Abdur Rahman Crescent Institute of Science and Technology, India

**Abstract** — Electric bicycles are becoming increasingly popular as green mobility solutions. However, problems of low mileage, a poor power factor, and unstable charging voltage still persist. This study proposes a novel power management system with a Super-Lift Converter (SLC), Field Programmable Gate Array (FPGA)-regulated active front-end circuitry, and a flexible solar panel to address the issues. The system's design uses a 350 W BLDC hub motor and a 36 V 10.4 Ah lithium-ion battery. A SLC is inserted between the charger and battery to achieve a high voltage transfer gain and voltage ripple of less than 1%. The incorporated FPGA runs an Adaptive Reinforcement-based Current Tracking (ARCT) algorithm to provide power factor correction by generating a synchronized reference inductor current with the input voltage waveform. A 60 W, 36 V flexible solar panel is attached to a secondary input of the SLC to provide solar-assisted charging and extend the vehicle range from 45 km to 50 km per charge. During charging of the 36–42 V lithium-ion battery, the system is powered from a 230 V AC grid, stepped down to 100 V AC using a transformer, along with the PV input. Experimental results attest to a dramatic reduction in total harmonic distortion and enhanced current

tracking performance. The proposed system provides a sustainable and compact solution for electric bicycles and similar energy-efficient mobility platforms.

**Index Terms** — Active front end, battery, electric bicycle, power factor correction, total harmonic distortion.

## I. INTRODUCTION

Electric bicycles (e-bicycles) are a future substitute for conventional vehicles and a cost-effective, green, and energy-efficient form of urban transportation. With the world focusing on sustainable transport, e-bicycles are gaining momentum in urban areas, particularly in short-distance trips. Range limitations due to inefficient charging and energy management systems are still a hindrance to their widespread adoption. Low battery life and low power quality during charging are serious issues [1]. Smart control techniques could improve autonomy and user experience, according to the evidence provided by an adaptive electric bicycle study [2].

The primary challenge is battery efficiency. Lithium-ion batteries typically used in e-bicycles are current- and voltage-ripple-sensitive during charging, and such ripples can accelerate degradation and decrease the cycle life. Conventional boost converters, although simple and inexpensive, tend to lack the high gain and low ripple in a single step. Inductive power transfer and wireless charging system solutions enabled new e-bicycle configurations [3]; however, these systems tend to add complexity and cost. Hybrid parallel topologies and optimized coil topologies for a stable current output in inductive charging systems were also investigated [4].

The performance of the charging system is directly related to energy usage and ride quality. For example, a

\* Corresponding author.  
E-mail: elangoeee2007@gmail.com

DOI: [10.25729/esr.2025.04.0009](https://doi.org/10.25729/esr.2025.04.0009)

Received July 13, 2025. Revised October 24, 2025. Accepted November 27, 2025. Available online December 29, 2025.

This is an open-access article under a Creative Commons Attribution-NonCommercial 4.0 International License.

© 2025 ESI SB RAS and authors. All rights reserved.

control-based hybrid bicycle test experiment verified the necessity of finding the optimal tradeoff between fuel economy and capacity loss [5].

More advanced power management strategies can optimize energy utilization. A reinforcement learning-based assisted power management system was proposed to enable real-time power sharing adaptation between motor and human inputs in e-bicycles [6]. These intelligent strategies are crucial for meeting the performance needs of users while respecting size, cost, and energy storage limitations. A double-wheel drive strategy to improve user experience in electrically assisted bicycles also showed the need for combined control [7].

Thus, an efficient and scalable charging infrastructure is critical for mass adoption. Extremely large inductive charging stations using hybrid topology switching and single inverters were studied to support a growing number of e-bicycles [8]. Hybrid topologies with configurable voltage and current outputs were reported to increase charging flexibility [9, 10]. Even cost-effective wireless charging systems were implemented to provide feasible solutions to customers [11]. These developments notwithstanding, challenges still exist as concerns the high power factor (PF), low total harmonic distortion (THD), and low ripple, particularly in compact systems.

FPGA-based control solutions are becoming increasingly prevalent in power electronics owing to their capability for real-time operation and reconfigurability. High-precision timing, real-time digital control for active power filters, and high-frequency GaN-based DC-DC converters were all improved through FPGA implementations [12–14]. Online inductance identification based on FPGA-based systems also underscored the platform's potential for power converter control in electric

vehicle (EV) systems [15].

Super-lift converter (SLC) topologies [16] proved useful for the high-voltage gain in low-ripple applications. In EV applications, advanced designs with buck converters or positive output lift stages can deliver higher voltage conversion efficiency and output quality [17, 18]. For example, a combination of Luo and Cuk topologies simplified the circuit, enhanced the gain, and enabled low-ripple operations [19]. Control strategies, such as the sliding mode and adaptive estimation, offer robust performance even in converter environments with uncertainties [20].

Adaptive control methods are crucial for systems that encounter model uncertainties, disturbances, or dynamic changes. Adaptively tuned current-mode control techniques and window-based mode selectors with adaptation improved the converter's response [21]. Adaptive perturbation rejection techniques and output feedback control also improved robust tracking and system stability [22]. These techniques became even more crucial in EV systems, where source and load conditions can change rapidly.

In recent years, there has also been increasing interest in reinforcement-learning (RL) driven controllers for power converters and EVs. RL-based controllers in power electronic applications were introduced with steady-state error compensation schemes [23], whereas deep RL were implemented for dynamic active and reactive power control of grid-connected EVs [24]. Predictive RL methods [25] and meta-RL current control schemes for motor drives [26] indicated the feasibility of RL under various converter conditions. Real-world applications include RL-driven buck converter control under time-delay conditions [27], smart MPPT controllers for renewables [28], and

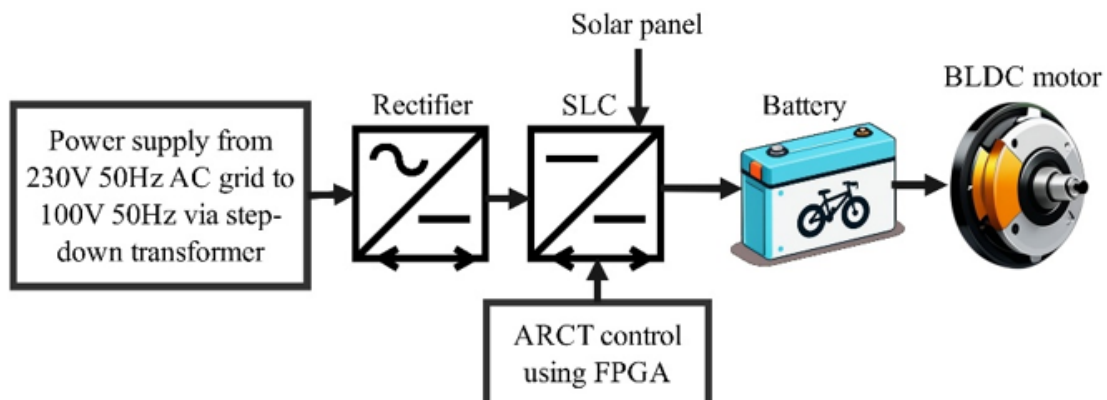


Fig. 1. Overall architecture of the proposed system.

stabilization of boost converters under CP loads through deep RL [29]. Most recently, safety-augmented and self-learning RL schemes were introduced for converter applications [30] and adaptive RL-driven PID controllers were used for multi-area power grids [31]. This demonstrates RL's capability for adaptability and application-performance optimization in power grids. Although these applications for the most part remain constrained by computational overhead, the lack of real-time FPGA-based implementation and limited optimization targets such as MPPT or converter stabilization give way to research evolution. Thus far no RL framework has been specifically adapted for e-bicycle platforms, which require compact implementation of hardware, converter gain, ripple, and simultaneous PF and THD compliance. Given this background, there is a pressing need for an FPGA-implemented adaptive RL approach capable of PF, THD, and ripple tradeoff under virtual AC–PV input and hybrid mode operations.

In addition, power quality problems [32] in battery charging from AC sources, such as PF degradation and high THD were reported. Various unidirectional non-isolated PFC converters offered exceptional size advantages, efficiency, and reduction in harmonic trade-offs [33]. It was suggested that high-current-density EV chargers employ modified PI controllers to enhance dynamic response [34, 35]. Second-harmonic current reduction methods were applied in two-stage PFC systems

to eliminate distortions [36].

To address these challenges, the present study introduces a Super-Lift Converter (SLC) controlled by an FPGA-based Adaptive Reinforcement-Based Current Tracking (ARCT) algorithm. The major contributions of this work are summarized as follows:

- A first-of-its-kind FPGA-implemented ARCT for an on-board e-bicycle charger integrating grid and PV power.
- The experimentally proven near-unity power factor (0.99) and very low input current THD (2.23%).
- Stabilization of PV output voltage under varying irradiance using combined MPPT–ARCT interaction within the SLC topology.
- Reduction of battery terminal ripple (<1.5%) and improved charging smoothness, supporting reduced degradation and extended cycle life.
- Demonstration of a practical hybrid e-bicycle platform with a 15% improvement in battery-supported mileage, validating the proposed control strategy.

## II. OVERALL E-BICYCLE SYSTEM ARCHITECTURE

The architecture of the hybrid charging and propulsion system of the e-bicycle proposed in this study is shown in Fig. 1. The system employs a stepped down single-phase 100 V, 50 Hz AC supply from a 230 V, 50 Hz AC grid using a step-down transformer, which is connected to a

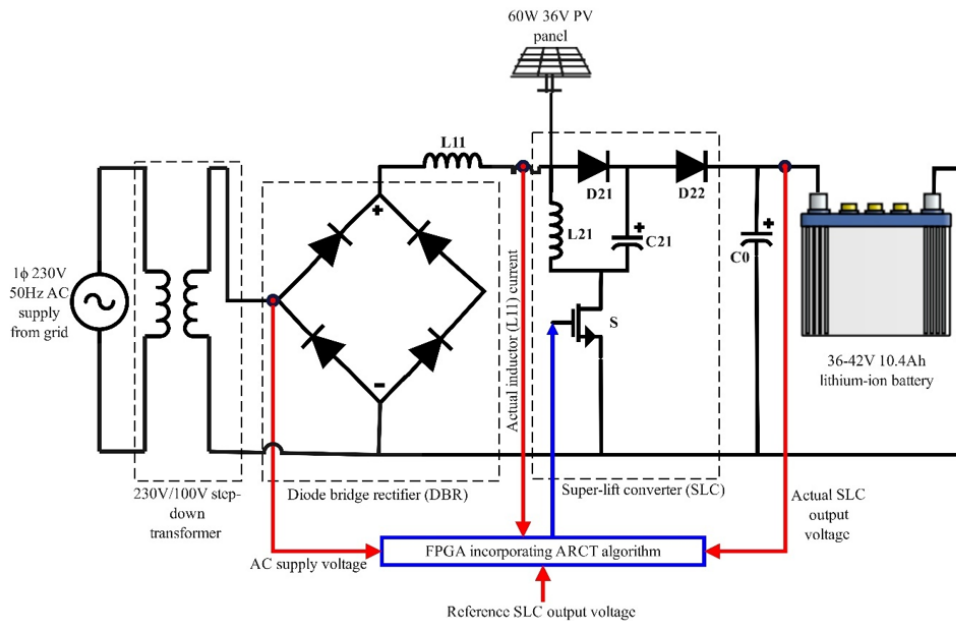


**Fig. 2. Detailed diagram of the designed system.**

TABLE 1. Nomenclature for the Proposed ARCT–SLC System

Variable	Description
$V_{in}$	Input AC voltage (after autotransformer)
$V_R$ & $I_R$	Rectified AC input voltage & current
$V_{PV}$ & $I_{PV}$	PV panel voltage & current
$V_{SLC}$	Average output voltage of SLC
$v_o$	Output/battery charging voltage
$i_L$	Inductor current
$\Delta$	Duty ratio generated by the actor network
$\theta$	Actor network weights
$\omega$	Critic network weights
$r[k]$	Reward at iteration k
$\delta[k]$	Temporal-Difference (TD) error
$\gamma$	Discount factor
$PF$	Power factor
$THD$	Total harmonic distortion
$V_{MPPT}$	PV voltage at MPP
$f_s$	Switching frequency
$T_s$	Sampling period
$N_{update}$	Actor-critic update interval
$\alpha_a, \alpha_c$	Learning rates for the actor and the critic

rectifier for AC-to-DC conversion.

The rectified supply is connected to a Super-Lift Converter (SLC), which is tailored to provide a high voltage gain with low output ripple. The converter is driven in a three-port configuration to facilitate the hybrid energy input and output. Port 1 is supplied with DC from the grid and is energized for indoor or stationary charging, whereas port 2 is linked to a flexible solar panel that supplies power during outdoor cycling. The solar panel is a 36 V, 60 W module. The SLC charges a 36–42 V, 10.4 Ah lithium-ion battery pack. Port 3 supplies the regulated DC output to charge the lithium-ion battery, which supplies a Brushless DC (BLDC) motor for propulsion. An FPGA controller driven by an Adaptive Reinforcement-Based Current Tracking (ARCT) algorithm regulates the switching actions of the converter to provide voltage stability, enhance the power factor, and minimize harmonic distortion. The hybrid integrated configuration enhances energy efficiency, provides grid compatibility, and enhances the mileage of the e-bicycle.

A detailed schematic of the system implementation is shown in Fig. 2, where each functional block is represented by its corresponding electrical component. The AC supply is connected to a Diode Bridge Rectifier (DBR), and its

output is filtered using an input inductor ( $L11$ ).

The SLC stage includes a switching device ( $S$ ), inductors ( $L11$  and  $L21$ ), diodes ( $D21$  and  $D22$ ), and capacitors ( $C21$  and  $C0$ ), designed to have a multi-stage boost topology. A 60 W solar panel is implemented in the input path of the converter, enabling auxiliary energy harvesting. The SLC regulated output is supplied to a 10.4 Ah, 36–42 V lithium-ion battery. The FPGA is supplied with feedback signals such as the AC supply voltage, actual and reference SLC output voltages, and the current flowing through inductor  $L11$ . Based on this feedback, the ARCT algorithm dynamically controls the switching of  $S$  for an efficient operation under various load and input conditions. The figure provides the rationale behind the design by showing how the control and power stages communicate at the circuit level, enabling the high-efficiency and reliable operation of the hybrid e-bicycle charging system.

Passive components, such as inductor and capacitor values, are derived based on standard ripple constraints. The inductor is sized by

$$di_L = \frac{V_R \Delta}{L f_s}, \quad (1)$$

where,  $di_L$  is the ripple current in inductors  $L11$  and  $L21$ ,  $V_R$  is the rectified AC input voltage,  $\Delta$  is the switching duty cycle, and  $f_s$  is the switching frequency. Considering that the ripple current in the inductors is limited to 20% of the average inductor current at a switching frequency of 20 kHz,  $L11$  and  $L21$  can be chosen as 100  $\mu$ H.

The capacitor is chosen by

$$dV_C = \frac{I_0 \Delta}{C f_s}, \quad (2)$$

where,  $dV_C$  is the ripple voltage in capacitor  $C0$  and  $I_0$  is the current through capacitor  $C0$ . Considering that the ripple voltage in the capacitor is limited to less than 1% of the output voltage,  $C0$  can be set to 470  $\mu$ F. Table 1 summarizes all mathematical symbols and parameter notations used in the ARCT-regulated SLC model to ensure clarity and consistency throughout the text.

### III. SUPER-LIFT CONVERTER (SLC)

The SLC topology is derived from the Luo converter family, where voltage boosting is achieved through the sequential discharging and charging of multiple capacitors and inductors. A schematic of the SLC and its equivalent operating state are shown in Fig. 3. The illustration includes the entire circuit setup, as well as the two

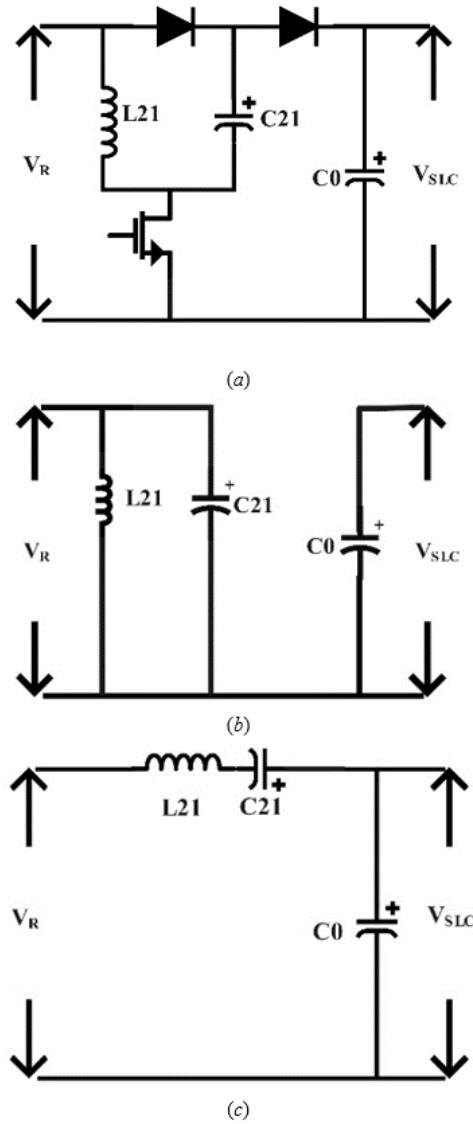


Fig. 3. (a) Overall circuit topology (b) Equivalent circuit when the switch is ON (c) Equivalent circuit when the switch is OFF.

prominent switching states, that is when the switch is ON and when the switch is OFF.

During the switch-ON interval, the DC link input energy of the switches is stored in inductor  $L_{11}$  and capacitor  $C_{21}$  is charged from the input voltage  $V_R$ , that is, the rectified voltage of a single-phase 100 V, 50 Hz AC source, by diode  $D_{21}$ . The energy is stored for a very short time interval in the magnetic field  $L_{11}$  and the electric field  $C_{21}$  and no energy is transferred to the output. When the switch is OFF, diode  $D_{21}$  is reverse-biased, diode  $D_{22}$  is forward-biased, and the stored energies of  $L_{11}$  and  $C_{21}$  are transferred to the output side through  $D_{22}$ , thereby boosting the voltage. The output capacitor  $C_0$  filters this energy and provides a smooth DC output voltage  $V_{SLC}$  between battery terminals.

This two-step energy-transfer process allows the converter to superimpose the voltage across  $C_{21}$  on top of the input voltage and generate a much higher output voltage. Not only does the operation increase the output, it also renders it low in ripple, which is a desirable characteristic for battery charging. Mathematical modeling of the voltage and current performance of the converter confirms this behavior. The average output voltage  $V_{SLC}$  of the SLC can be expressed as

$$V_{SLC} = \frac{2-\Delta}{1-\Delta} V_R, \tag{3}$$

where,  $V_R$  is the rectified AC input voltage, and  $V_{SLC}$  is the output voltage. Compared to the existing boost converter,

which has a gain of  $\frac{1}{2-\Delta}$ , the SLC has improved gain characteristics for the same switching duty cycle.

Similarly, the converter output current  $I_{SLC}$  can be defined in terms of the input current  $I_R$  as

$$I_{SLC} = \frac{1-\Delta}{2-\Delta} I_R. \tag{4}$$

The front end of the SLC is a full wave diode bridge rectifier (DBR) and its average output voltage is given by

$$V_R = \frac{2V_p}{\pi}, \tag{5}$$

where,  $V_p$  is the peak value of supply AC voltage.

Substituting equation (5) in (3), we get

$$V_{SLC} = \frac{2-\Delta}{1-\Delta} \cdot \frac{2V_p}{\pi}. \tag{6}$$

This expression ensures that the SLC effectively converts the voltage and current levels without disturbing the balance of energy and with minimal losses. The voltage transformation gain  $M$  is expressed as follows:

$$M = \frac{V_{SLC}}{V_R} = \frac{2-\Delta}{1-\Delta}. \tag{7}$$

The gain feature is much better than that of the conventional boost converter, especially for high duty cycle  $\Delta$  values; therefore, the SLC is ideal for high-voltage, low-ripple battery charging.

The use of more than one lifting stage, along with a voltage boost provides seamless conduction on the input side, enabling an improved power factor and reduced harmonic distortion. Such characteristics are inherent in applications where the input supply is an AC grid and power quality needs to be guaranteed. Additionally, because of its mode of operation, the SLC inherently provides low electromagnetic interference (EMI) and reduced stress on the switch, thereby improving the system reliability and component life.

In the proposed system, the SLC is interfaced with an FPGA that implements an ARCT algorithm. The ARCT controller dynamically adjusts the duty cycle of switch  $S$  based on the real-time measurement of the inductor current and input voltage. The control causes the inductor current to follow a sinusoidal reference, essentially performing power factor correction at the input and stable charging at the output. The SLC with the ARCT algorithm achieves voltage step-up and intelligent control, resulting in a compact, adaptive, and grid-connected charging compliant system.

Thus, SLC simplifies the hardware and facilitates high-performance control integration. Its inherent high-gain characteristic, low output ripple, and compatibility with advanced digital control techniques, such as ARCT, make it a good choice for modern EV battery chargers. The next

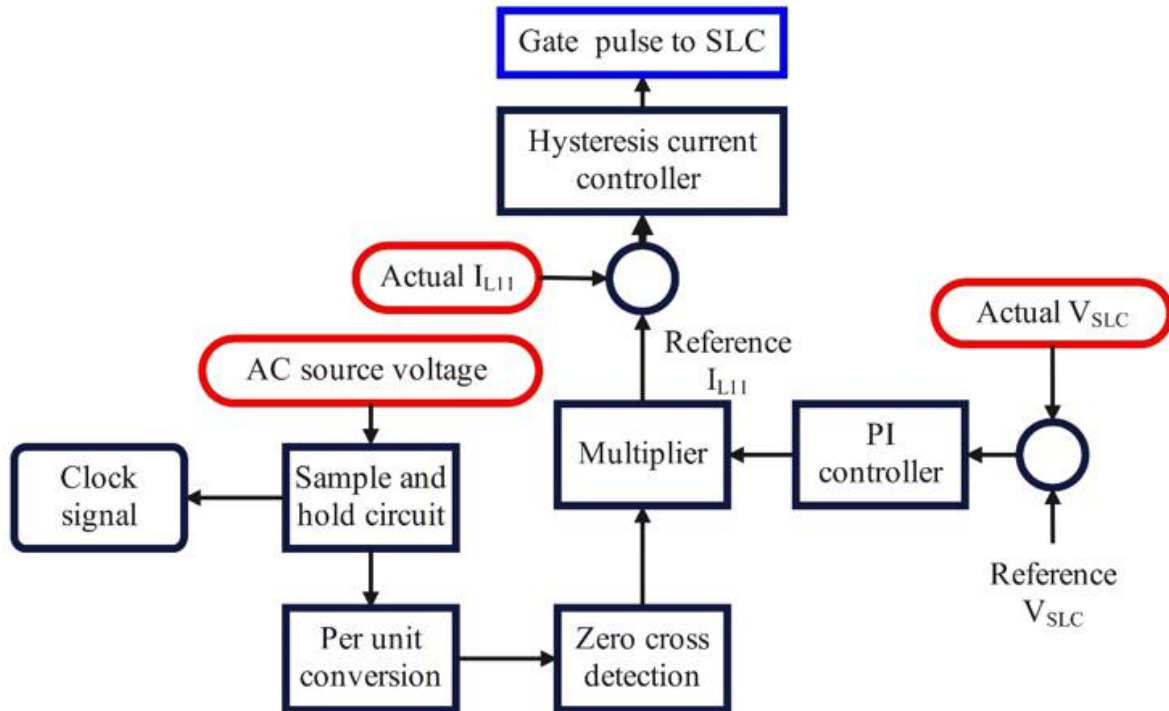


Fig. 4. Proposed ARCT architecture.

section discusses the ARCT algorithm, which controls the SLC operation to provide optimal current tracking and enhanced power quality.

#### IV. DESIGN FRAMEWORK OF THE ARCT ALGORITHM

The proposed ARCT configuration shown in Fig. 4 combines the high-voltage gain benefit of the Super-Lift Converter (SLC) with an adaptive reinforcement learning-based current tracking methodology to achieve improved power quality and battery charging stability.

The ARCT algorithm is based on the actor-critic reinforcement learning framework, which is defined by two primary components: the actor and the critic. The actor is responsible for selecting control actions (i.e., the switch duty cycle in the SLC), and the critic evaluates the quality of the action chosen by running a reward function based on the system response with special emphasis on inductor current tracking. The control objective is to condition the input current to follow a sinusoidal reference waveform in phase with the input voltage to achieve power factor correction and reduce the total harmonic distortion (THD).

The inductor current  $i_L(t)$  is measured at each sampling instant and compared with the synthesized reference current  $i_{L,ref}(t)$ , which is generated as a scaled input rectified voltage.

The error is computed as follows:

$$e(t) = i_{L,ref}(t) - i_L(t). \quad (8)$$

The critic network approximates the estimated return using the estimate function  $V(s_t)$ , where  $s_t$  is the current state of the system.

The temporal-difference (TD) error signal is computed as

$$\delta(t) = r(t) + \gamma V(s_{t+1}) - V(s_t), \quad (9)$$

where,  $\gamma \in (0, 1]$  is the discount factor, and  $s_t + 1$  is the next state considered as a consequence of applying the selected control action. The TD error is the error in the estimation of the reward and is what the actor and critic are updated with.

The actor network, responsible for generating the duty cycle  $d(t)$ , generates a control action based on a parameterized policy function  $\pi_\theta(s_t)$ , given by

$$d(t) = \pi_\theta(s_t) = \theta^M \phi(s_t). \quad (10)$$

Here,  $\theta$  is the actor parameter vector, and  $\phi(s_t)$  is the system state feature representation. The actor parameters are learned by the policy gradient method, which adjusts the control policy to maximize the expected reward:

$$\theta \leftarrow \theta + \alpha_a \delta(t) \nabla_\theta \log \pi_\theta(s_t), \quad (11)$$

where  $\alpha_a$  is the actor's learning rate. Simultaneously, critic parameters  $\omega$ , used for approximating  $V(s_t)$ , are updated to minimize the mean-squared TD error:

$$\omega \leftarrow \omega + \alpha_c \delta(t) \nabla_\omega V(s_t), \quad (12)$$

where  $\alpha_c$  is the critical learning rate. Control action  $d(t)$  is then converted into a gate signal for the power switch in the SLC. As the ARCT algorithm learns and adapts over time, the converter can dynamically switch the switching action to accurately follow the current, improve the input power factor, and minimize the harmonic distortions without system modeling or fixed control laws.

The strength of the ARCT approach is its generalization across the operating points. Unlike fixed-gain controllers that require re-design for different supply voltage or load levels, the actor-critic policy learns an optimal action across a wide range of conditions via reinforcement learning. Furthermore, the actor-critic architecture is a trade-off between learning stability and responsiveness and can be readily implemented at high speed in an embedded system on an FPGA platform.

The ARCT controller is implemented in discrete-time with the sampling time synchronized with the converter PWM switching frequency. It receives the sensed inductor current and supply voltage for each switching cycle, computes the control policy, updates the weights through gradient-based computations, and utilizes the updated duty cycle for the subsequent switching period. The reference current waveform  $i_{L,ref}(t)$ , is furnished by a zero-cross detection circuit and scaled in proportion to the instantaneous rectified AC input such that the input current is sinusoidal and in phase with the source voltage.

#### V. MATHEMATICAL MODELING AND THEORETICAL VALIDATION

The proposed Adaptive Reinforcement-Based Current Tracking (ARCT) algorithm employs an actor-critic reinforcement learning framework to regulate the SLC for lithium-ion battery charging from hybrid power sources. A thorough mathematical model of the system, where theoretical and experimental values are compared, such as power factor (PF), total harmonic distortion (THD), inductor current tracking, battery ripple voltage, and stable photovoltaic (PV) output is described below.

The total source current can be represented as

$$i_m(t) = i_L(t) + \sum_{n=2}^{\infty} \left( \frac{V_{in}}{nZ_n} \sin(n\omega t + \Phi_n) \right) = i_{L,ref}(t) + e(t), \quad (13)$$

where,  $i_{in}(t)$  is the source current,  $i_L(t)$  is the inductor current,  $V_{in}$  is the supply voltage,  $Z_n$  is the  $n$ -th harmonic impedance,  $\omega$  is angular frequency,  $\Phi_n$  is the phase angle of the  $n$ -th harmonic,  $i_{L,ref}(t)$  is the reference inductor current, and  $e(t)$  is the tracking error.

The dynamic voltage transfer gain of the SLC can be expressed as

$$M(t) = \frac{V_{SLC}}{V_R} = \frac{(2 - \Delta(t))^2 + k_1 e^2(t)}{(1 - \Delta(t)) \left(1 + k_2 \frac{d\Delta(t)}{dt}\right)}, \quad (14)$$

where,  $M(t)$  is the instantaneous gain,  $\Delta(t)$  is the duty ratio,  $e(t)$  is the tracking error,  $k_1$  and  $k_2$  are tuning constants.

The total harmonic distortion (THD) can be expressed by

$$I_{in,RMS} = \sqrt{I_1^2 + \sum_{n=2}^N I_n^2}, \quad (15)$$

$$THD = \left( \frac{I_{in,RMS}^2 - I_1^2}{I_1^2} \right)^{\frac{1}{2}} \times 100\%,$$

where,  $I_{in,RMS}$  is the RMS input current and  $I_1$  is the fundamental component.

The stabilized PV output current is derived from:

$$I_{PV}(t) = \frac{V_{MPPPT}(t)}{R_{PV}} + \alpha_{pv} \sin(\omega_{sun} t) - \beta_{pv} e(t), \quad (16)$$

where,  $I_{PV}(t)$  is the PV current,  $V_{MPPPT}(t)$  is the maximum power point voltage,  $R_{PV}$  is the panel resistance,  $\omega_{sun}$  is the solar frequency component,  $\alpha_{pv}$ , and  $\beta_{pv}$  are the control gains.

Ripple voltage at the battery terminal can be estimated by

$$\Delta V_{batt}(t) = \left[ \frac{1}{C_{batt}} \int_0^T \left( I_{batt}(t) - \frac{V_{batt}(t)}{R_{int}} \right) dt \right] + \gamma \frac{d\Delta(t)}{dt}, \quad (17)$$

where,  $\Delta V_{batt}(t)$  is the ripple voltage,  $C_{batt}$  is the battery capacitance,  $I_{batt}(t)$  is the battery charging current,  $V_{batt}(t)$  is the terminal voltage,  $R_{int}$  is the internal battery resistance, and  $\gamma$  is the tuning constant.

The duty cycle generated by the actor network is

$$\Delta(t) = \sigma(W_a^T \Phi(s_t) + b) + \lambda \delta(t), \quad (18)$$

where,  $\sigma$  is the activation function,  $W_a$  is the actor weight vector,  $\Phi(s_t)$  is the feature vector of state  $s_t$ ,  $b$  is the bias,  $\lambda$  is the learning rate, and  $\delta(t)$  is TD error.

The reward function used by the ARCT agent is given by

$$r(t) = -[\alpha_1 e^2(t) + \alpha_2 (1 - PF)^2 + \alpha_3 THD^2], \quad (19)$$

where,  $\alpha_1$ ,  $\alpha_2$ , and  $\alpha_3$  are weight constants, and PF and THD

are the performance metrics. The long-term voltage stability of the battery output is ensured if

$$\lim_{T \rightarrow \infty} \frac{1}{T} \int_0^T |V_{batt}(t) - V_{ref}| dt \leq 0.01 V_{ref}, \quad (20)$$

where,  $V_{ref}$  is the reference terminal voltage.

The critic update includes PV regulation as

$$\nabla_{\omega} V(s_t) = \nabla_{\omega} \left( \sum_{j=1}^n \omega_j \Phi_j(s_t) + \xi |I_{PV}(t) - I_{PV,ref}| \right), \quad (21)$$

where,  $V(s_t)$  is the critic value,  $\omega_j$  are weights,  $\Phi_j(s_t)$  are features, and  $\xi$  is the PV error penalty.

The net energy transferred to the battery is modeled by

$$E_{batt,total} = \int_0^T (\eta_{AC} P_{AC}(t) + \eta_{PV} P_{PV}(t)) dt - \int_0^T P_{loss}(t) dt, \quad (22)$$

where,  $\eta_{AC}$  and  $\eta_{PV}$  are the efficiencies of AC and PV paths, respectively,  $P_{AC}$  and  $P_{PV}$  are the input powers, and  $P_{loss}$  is the total converter loss. These equations provide theoretical backing to broadly explain the experimental results.

The proposed ARCT controller for SLC is implemented on an FPGA platform to ensure real-time operation and fast adaptability. The control process operates on a discrete-time scale synchronized with the switching frequency of the power converter. The switching stage is driven by the unipolar PWM at switching frequency  $f_s = 20$  kHz. The triangular carrier for PWM has a frequency  $f_s$  and peak amplitude 1. The duty command  $\Delta[k]$  (discrete-time index  $k$ ) is translated to gate pulses by comparing  $\Delta[k]$  with the carrier. The switch is ON when  $\Delta[k] > carrier(t)$  and OFF otherwise. The control loop runs at the sampling frequency  $f_s$  and the sampling period is 50  $\mu$ s. All sampled signals are filtered before digitization by a first-order anti-aliasing filter with the cutoff at  $f_c$ , which is one-fourth of  $f_s$ . Signals on the FPGA are represented in the fixed-point Q1.15 format (16-bit signed) to satisfy the timing and resource constraints.

#### A. TD Error Formulation

To make the ARCT algorithm explicit, the discrete-time temporal-difference error (TD error) used by the critic is implemented as

$$\delta(k) = r[k] + \gamma V_{\omega(s[k+1])} - V_{\omega(s[k])}, \quad (23)$$

where  $\delta[k]$  is the TD error at sample  $k$ ,  $r[k]$  is the scalar reward at sample  $k$ ,  $\gamma$  is the discount factor,  $V_{\omega(\cdot)}$  is the critic value function parameterized by weight vector  $\omega$ , and  $s[k]$  is the system state vector at time-step  $k$ . The state vector is chosen as follows:

$$s[k] = [i_{L[k]}, V_{R[k]}, V_{SLC[k]}, i_{PV[k]}]^T, \quad (24)$$

where  $i_L$  is the measured inductor current,  $V_R$  is the rectified DC input (per unit),  $V_{SLC}$  is the SLC output/battery terminal voltage, and  $i_{PV}$  is the PV current.

### B. Reward Function

The actor outputs a continuous duty command from a lightweight neural policy (one hidden layer) and is updated online using the policy-gradient style rule:

$$\theta[k+1] = \theta[k] + \alpha_a \delta(k) \nabla_{\theta} \pi_{\theta}(s[k]), \quad (25)$$

where  $\theta[k]$  is the actor parameter vector at the  $k^{\text{th}}$  step,  $\alpha_a$  is the actor learning rate,  $\delta[k]$  is the temporal difference (TD) error,  $\pi_{\theta}(s[k])$  is the policy function parameterized by  $\theta$ , evaluated at state  $s[k]$ ,  $\nabla_{\theta}$  denotes the gradient with respect to actor parameters.

### C. Critic Update

The actor output is saturated to enforce safe switching,

$$\Delta[k] = \text{saturate}(\pi_{\theta}(s[k]), \Delta_{\min}, \Delta_{\max}), \quad (26)$$

where  $\Delta_{\min} = 0.15$  and  $\Delta_{\max} = 0.85$  in our implementation. The critic is updated using a semi-gradient TD (0) update implemented as follows:

$$\omega[k+1] = \omega[k] + \alpha_c \times \delta(k) \times \nabla_{\omega} V_{\omega}(s[k]), \quad (27)$$

where  $\alpha_c$  is the critic learning rate and  $\nabla_{\omega} V_{\omega}$  is the gradient of the critic value function.

### D. Actor Update

The reward used for online learning is a normalized negative quadratic that balances the current tracking, power quality, and output regulation:

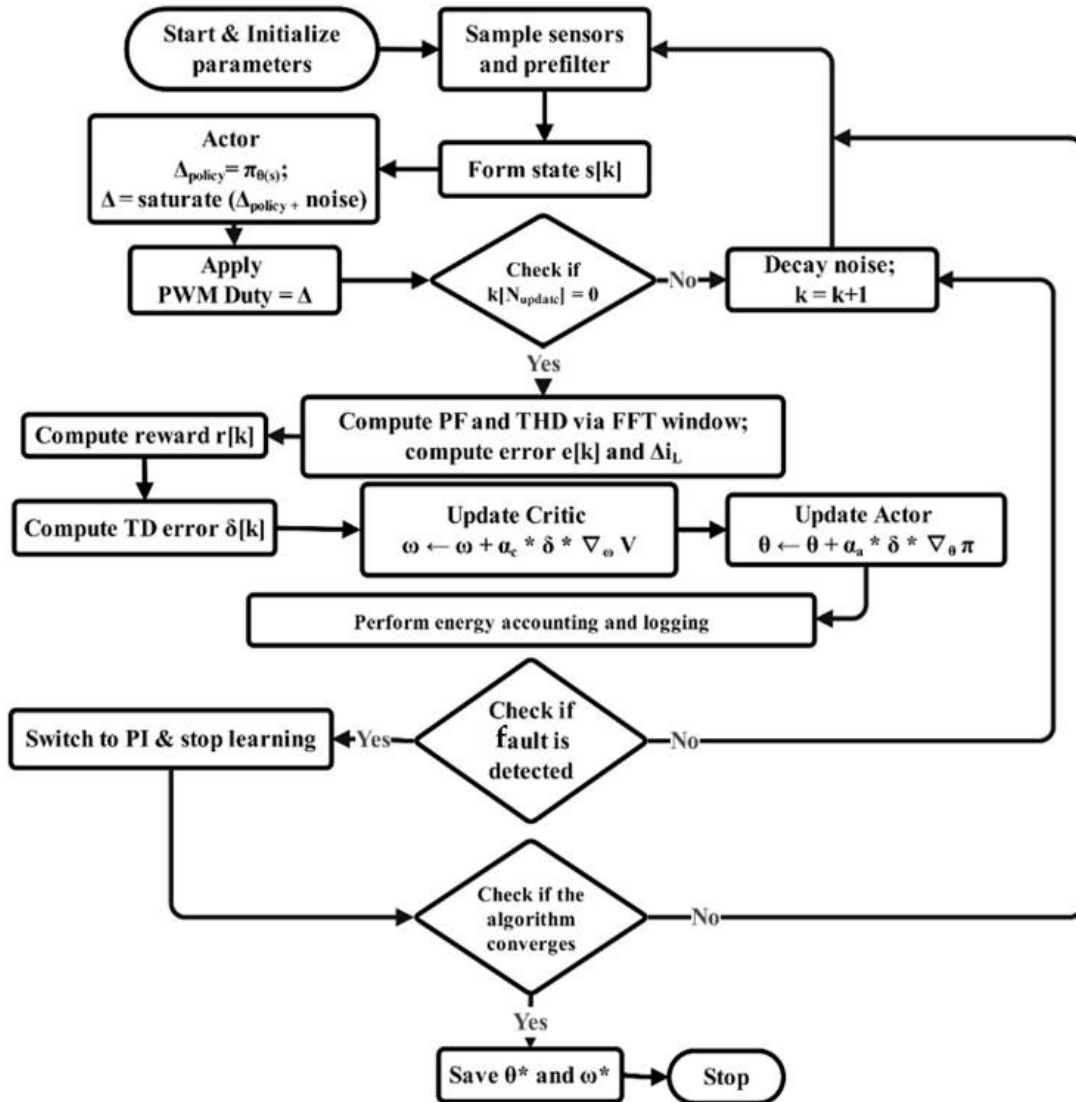


Fig.5. Adaptive reinforcement-based current tracking (ARCT) learning mechanism.

$$r[k] = -[\alpha_1 e^2[k] + \alpha_2 (1 - PF[k])^2 + \alpha_3 THD[k]^2 - \alpha_4 (V_{SLC}[k] - V_{ref})^2 + \alpha_5 \Delta i_{L[k]}^2], \quad (28)$$

where  $e[k] = i_{L,ref}[k] - i_L[k]$  is the inductor current tracking error,  $PF[k]$  is the instantaneous power factor estimate (per unit),  $THD[k]$  is the short-time THD estimate (per unit) computed over the last  $M$  samples,  $V_{ref}$  is the target battery charge voltage,  $\Delta i_L[k]$  is the inductor ripple estimate, and  $\alpha_1 - \alpha_5$  are scalar reward weights. Short-time THD and PF are computed using an  $N$ -sample sliding window FFT on the FPGA host (or on a connected controller) as follows:

$$THD[k] = \frac{\sqrt{\sum_{n=2}^{N_h} I_n^2}}{I_1}, \quad (29)$$

$$PF[k] = \frac{\frac{1}{T_\omega} \sum_{t=k-T_\omega+1}^k V_R(t) i_R(t)}{\sqrt{\frac{1}{T_\omega} \sum_{t=k-T_\omega+1}^k V_R(t)^2} \sqrt{\frac{1}{T_\omega} \sum_{t=k-T_\omega+1}^k i_R(t)^2}}, \quad (30)$$

where  $I_n$  are harmonic magnitudes of the input current computed from the short window FFT ( $N_h$  harmonics used; we use  $N_h = 40$ ),  $I_1$  is the fundamental, and  $T_\omega$  is the window length in samples. The FFT window uses a

TABLE 2. Learning Hyper-Parameters

Component/Parameter	Specification
Switching frequency ( $f_s$ )	20 kHz
Sampling period ( $T_s$ )	50 $\mu$ s
Discount factor ( $\gamma$ )	0.95
Actor learning rate ( $\alpha_a$ )	0.01
Critic learning rate ( $\alpha_c$ )	0.005
Reward weights	0.5, 0.3, 0.2
PV penalty factor ( $\xi$ )	0.1
Duty ratio limits ( $\Delta_{min}, \Delta_{max}$ )	0.1, 0.9

Hanning window and energy is computed up to the 40<sup>th</sup> harmonic to match the IEEE harmonics standard. To limit online computation on the FPGA, the actor is evaluated every control cycle, while the critic weight updates and RMS/FFT-based PF/THD calculations are performed every  $N_{update}$  cycles. This reduces resource usage while preserving control responsiveness.

The learning process of the ARCT controller is shown in Fig. 5. The actor network generates the control duty ratio  $\Delta(k)$  based on the observed converter state  $s(k)$ . The critic network evaluates the temporal-difference (TD) error  $\delta(k)$ .



Fig. 6. View of the designed e-bicycle.

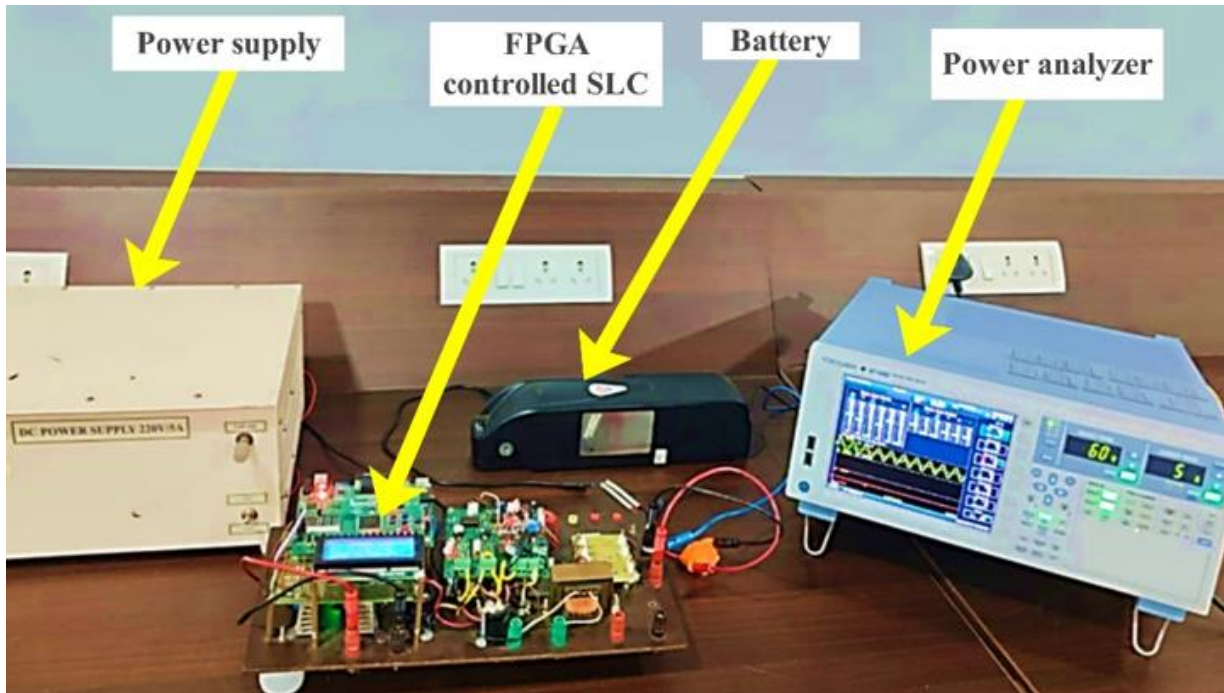


Fig. 7. Test bed of the incorporated super-lift converter.

Both networks update their parameters in real time according to the weight-update rule of Eq. (27) and Eq. (28).

The actor weights  $\theta$  are adjusted to minimize the error between the reference inductor current and the measured value, while the critic weights  $\omega$  estimate the long-term performance value.

This cooperative interaction enables adaptive duty-cycle regulation that yields ripple-free current tracking and improved PF correction under varying load and irradiance conditions. The learning hyper-parameters used in our experiments are summarized in Table 2.

## VI. EXPERIMENTAL VALIDATION

To validate the performance of the proposed battery charging system using the SLC regulated by the ARCT algorithm, a hardware prototype was developed and tested. Figure 6 shows the designed e-bicycle with a hybrid charging system. The 10.4 Ah lithium-ion battery is placed on the middle frame to obtain the weight distribution balance. A solar panel is placed on the rear carrier with a cabinet design and flexible openings. The SLC and FPGA-based control circuitry are placed inside the solar panel cabinet for compactness. The BLDC hub motor is placed

on the rear wheel to ensure smooth and efficient propulsion.

The test bed of the proposed ARCT-based FPGA-controlled SLC is shown in Figure 7. The experimental parameters for the proposed system are listed in Table 3.

The power factor (PF) and total harmonic distortion (THD) of the proposed hybrid e-bicycle charging system were experimentally evaluated using a Yokogawa WT1800E precision power analyzer, which complies with

TABLE 3. Experimental Parameters

Component/Parameter	Specification
AC input voltage	230 V RMS, 50 Hz
Input rectifier	Single-phase full-bridge diode rectifier
Battery capacity	10.4 Ah, 36–42 V lithium-ion battery
SLC inductor $L11, L21$	100 $\mu$ H each
Capacitor $C21, C0$	470 $\mu$ F / 63 V low-ESR electrolytic capacitors
Power switch	IRF540N MOSFET (100 V, 33 A, $R_{DS(on)} \{DS(on)\} = 0.044 \Omega$ )
Diodes $D21, D22$	Fast recovery diodes (UF4007 or MUR460 equivalents)
Control platform	FPGA-based custom controller
Sensor interfaces	Hall-effect voltage and current sensors

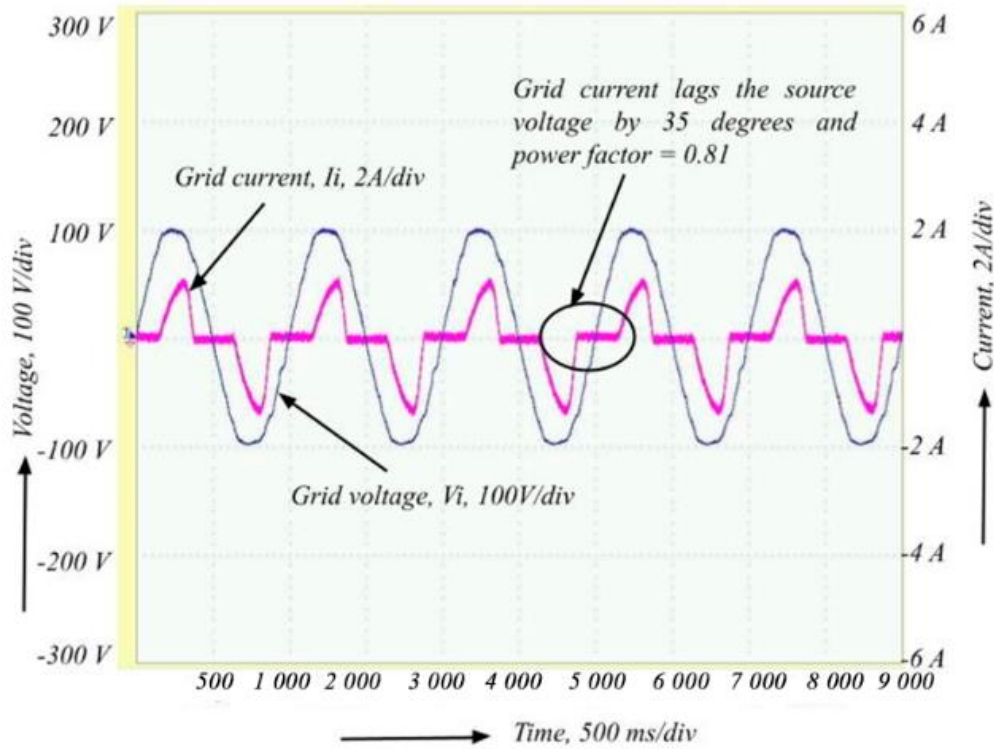


Fig. 8. Supply voltage and current without ARCT.

IEC/IEEE measurement standards. The analyzer was configured with a sampling frequency of 200 kHz and a measurement window synchronized with the fundamental

grid frequency (50 Hz). For THD estimation, the Fast Fourier Transform (FFT) method was applied with a Hanning window, and harmonics up to the 40<sup>th</sup> were

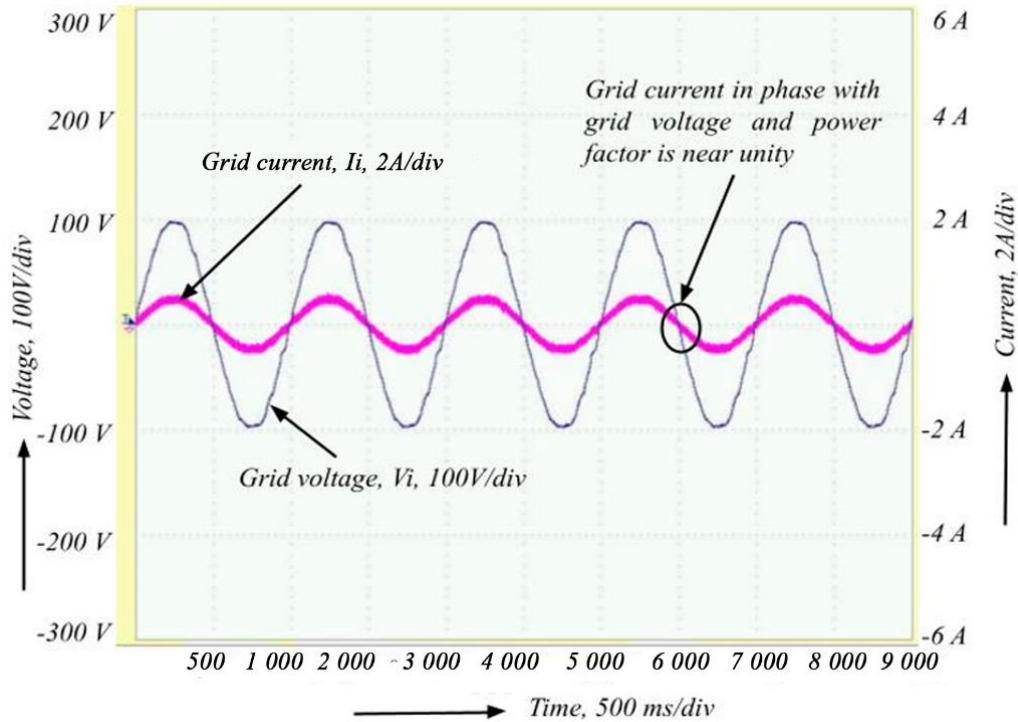


Fig. 9. Supply voltage and current with ARCT.

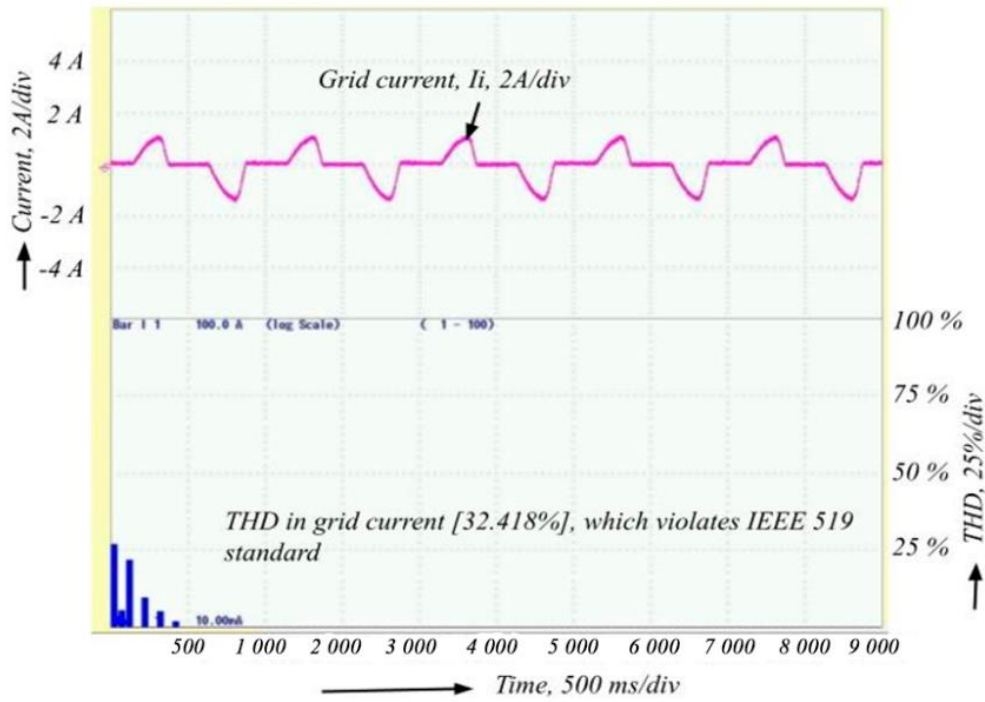


Fig. 10. THD in supply current without ARCT.

TABLE 4. THD Order and Current Without ARCT

Harmonic order	1	3	5	7	9	11	13
Grid current, A	0.2146	0.0565	0.0085	0.0027	0.0009	0.0003	0.0002

considered, as recommended by IEEE Std. 519-2014. The experimental results shown in Fig. 8–20 reveal significant

improvements achieved with the aid of the proposed system. Figure 8 represents the supply voltage and current

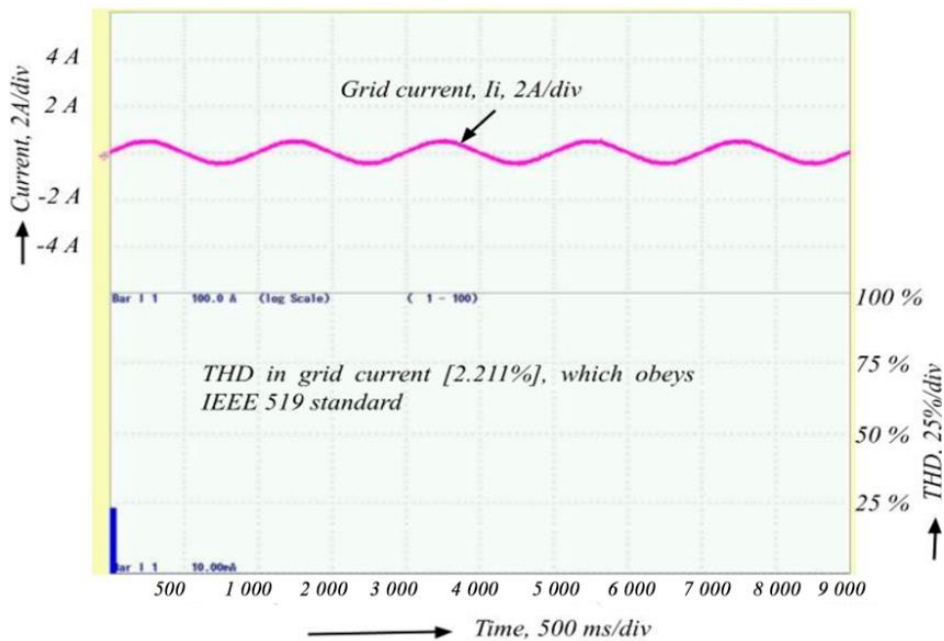


Fig. 11. THD in supply current with ARCT.

TABLE 5. THD Order and Current with ARCT

Harmonic order	1	3	5	7
Grid current, A	0.205	0.0002	0.001	0.001

waveforms during the charging of the battery without ARCT control. Without ARCT, there was a noticeable phase displacement between the current and voltage, indicating a poor power factor.

On the other hand, the waveforms were nearly in phase with the incorporation of ARCT control as shown in Fig. 9. This synchronization effectively enhanced the power factor and reduced the reactive power loss.

Figure 10 shows the Total Harmonic Distortion (THD) of the supply current in the absence of the proposed ARCT control. The harmonic order and the corresponding harmonic current values are summarized in Table 4. The current values up to the 13<sup>th</sup> harmonic, were measured and presented because the harmonics current was zero for harmonics above the 13<sup>th</sup>. The THD without ARCT control

was 32.418%, which exceeded the acceptable limits set by the IEEE 519 standard.

According to IEEE 519-2014, the allowable current THD limit is 5% at the Point of Common Coupling (PCC). The high THD in the absence of ARCT indicates reduced equipment life and increased power loss. When the proposed ARCT control is implemented, the THD is significantly reduced to 2.211% (as shown in Fig. 11), which complies with the IEEE 519 standard and ensures a better power quality. The harmonic order and the corresponding harmonic current values are summarized in Table 5. The current values up to the 7<sup>th</sup> harmonic were measured and presented because the harmonics current was zero for harmonics above the 7<sup>th</sup>. This ensures the proper

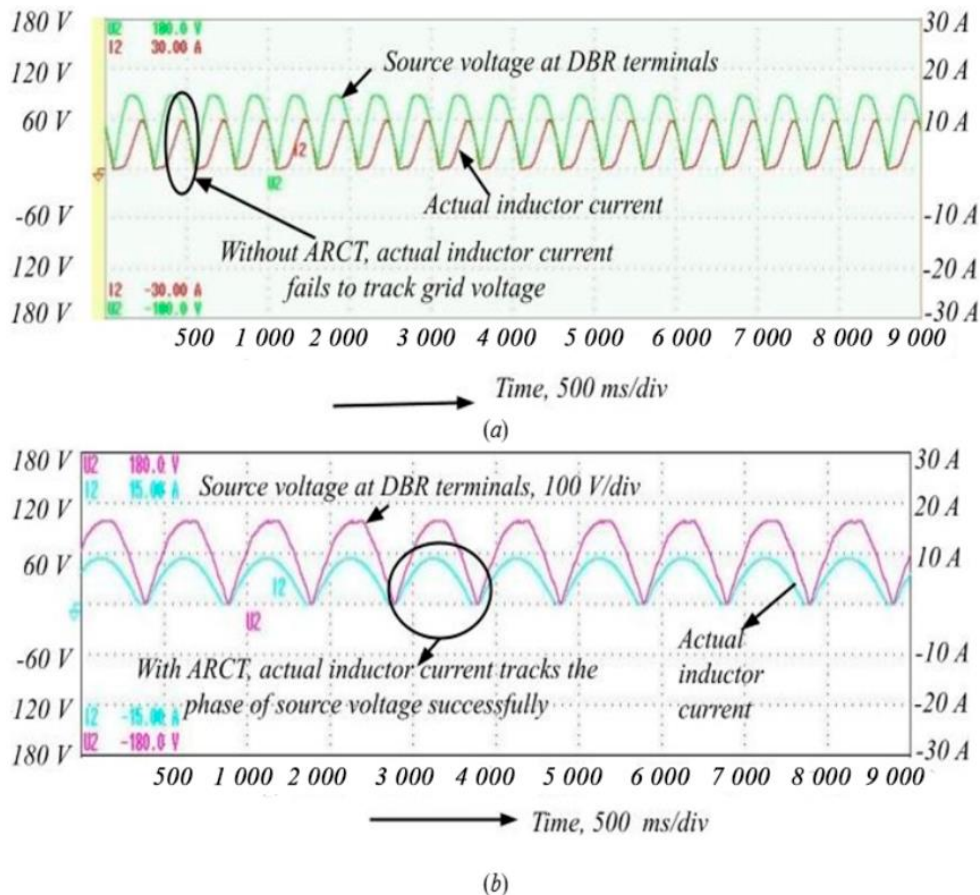


Fig. 12. Actual inductor current and source voltage at DBR terminals (a) without ARCT (b) with ARCT.

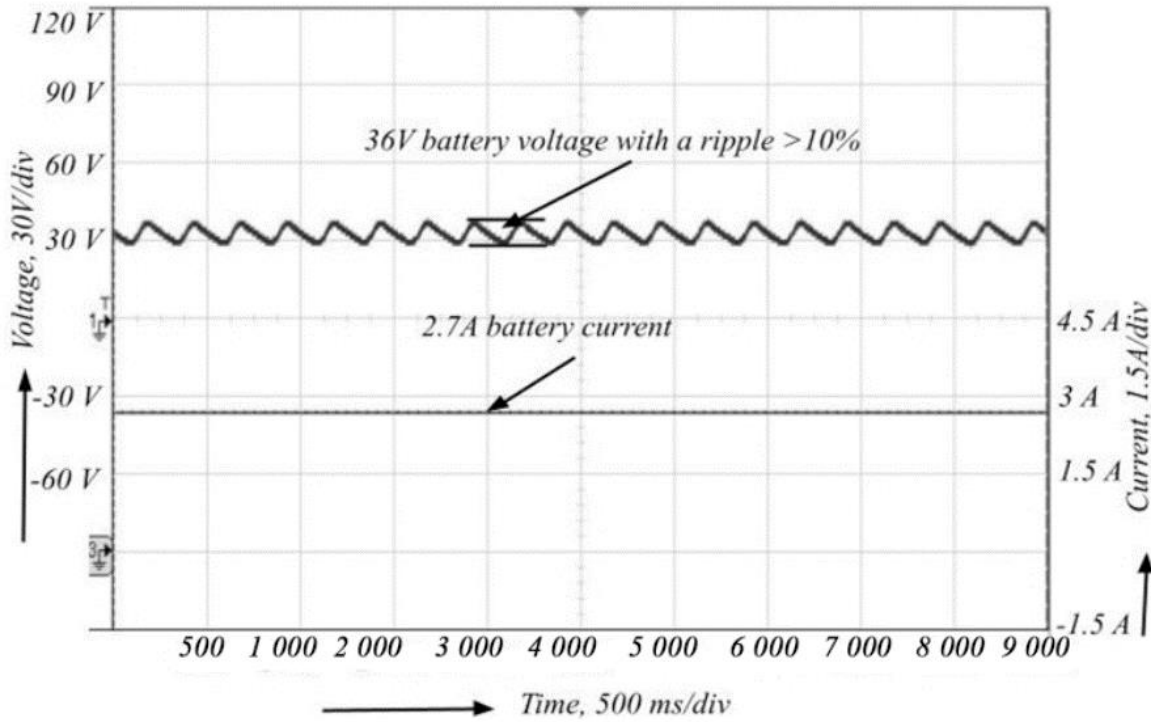


Fig. 13. Voltage and current in battery terminals without ARCT.

alignment of the supply current with the voltage waveform and minimizes harmonic distortions.

Figure 12 presents the waveforms of the source voltage at DBR terminals and actual inductor currents. Without ARCT control, there is a clear deviation of the actual

inductor current from the voltage signal, resulting in inefficient current tracking and higher ripples. By contrast, with ARCT control, the actual inductor current closely aligns with the source voltage at DBR terminals, which validates the implementation of the ARCT algorithm leading to improved stability and reduced ripple.

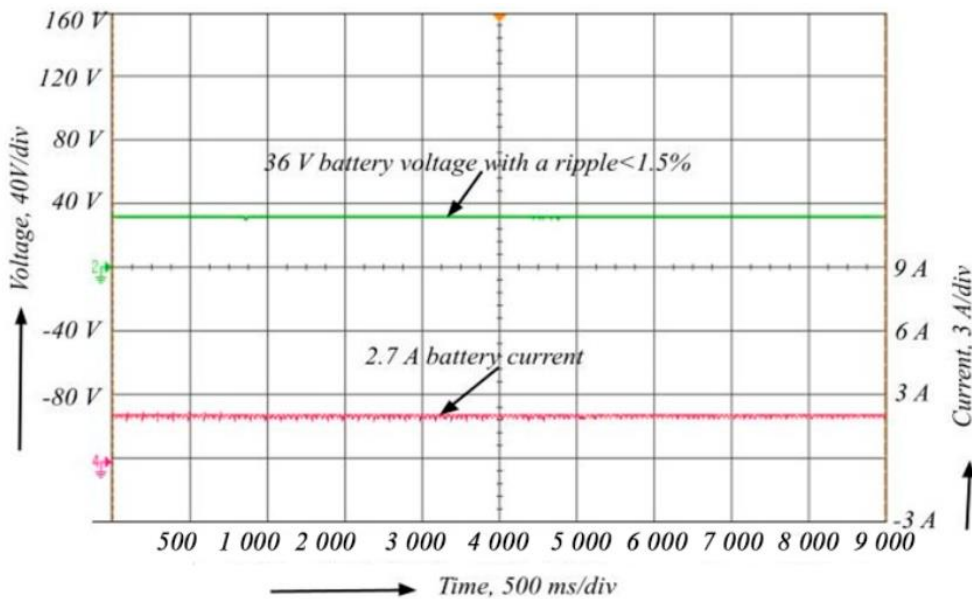


Fig. 14. Voltage and current in battery terminals with ARCT.

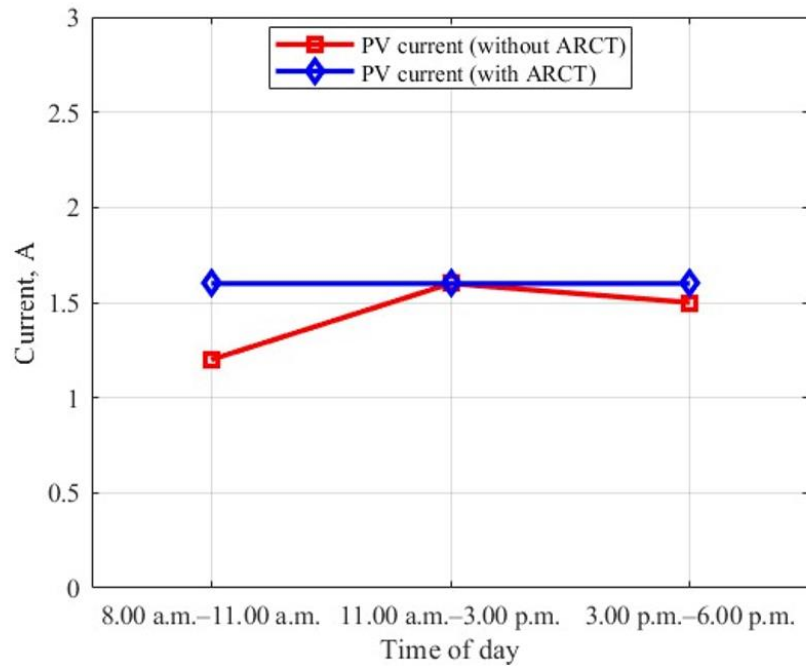


Fig. 16. PV output current with and without ARCT control.

Fig. 13 illustrates the voltage and current profiles at the battery terminals without ARCT control.

In the absence of ARCT control, the voltage at the battery terminals exhibited a ripple exceeding 10%, which compromised the charging process by introducing inefficiencies and potentially degrading the battery over

time. The current profile also shows significant fluctuations owing to the high ripple voltage, resulting in uneven charging and reduced battery life. Conversely, with the implementation of ARCT control (Fig. 14), the ripple voltage was significantly reduced to less than 1%, thus emphasizing that harmonic distortion was limited.

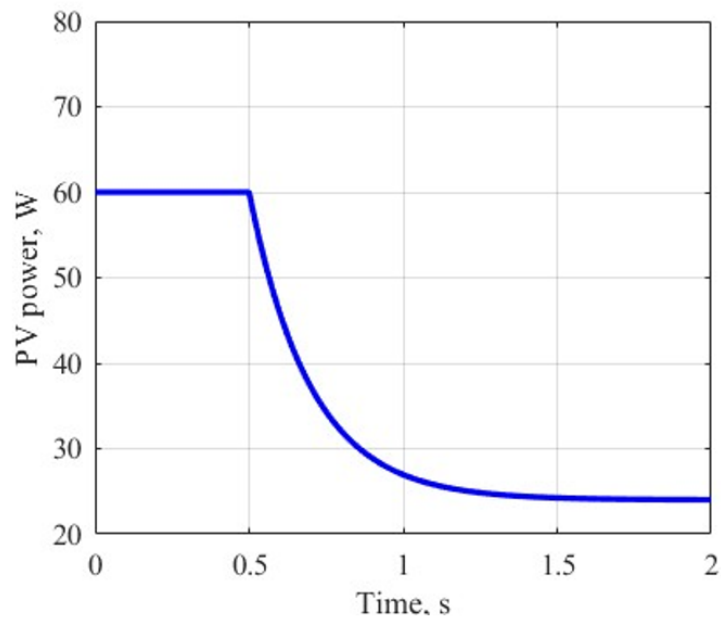


Fig. 17. MPPT dynamic response (1000→400 W/m²).

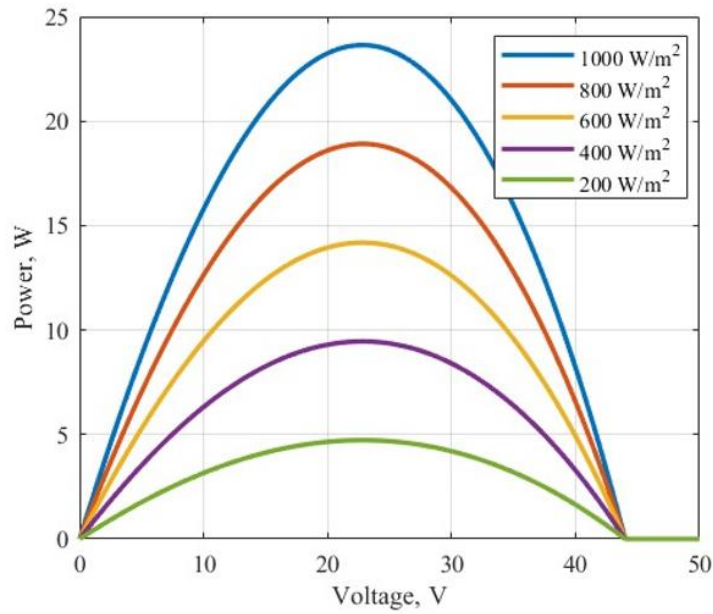


Fig. 18. P-V curves at 25°C.

Figure 15 shows the variability of the PV output voltage over different time ranges of the day, with and without ARCT control.

In the absence of the ARCT, the current oscillated with solar irradiance changes — 1.2 A in the morning (8:00–11:00 a.m.), 1.6 A at noon (11:00 a.m.–3:00 p.m.), and 1.5 A in the late afternoon (3:00–6:00 p.m.). These small oscillations demonstrate a lack of voltage control, with

suboptimal current generation under changing sunlight conditions. With the ARCT algorithm, the output current is maintained at 1.6 A over all periods. This stability demonstrates the ARCT’s capability to control the duty cycle of the converter and keep the operating point close to optimal, even with changing solar input. The regulated current improves the battery charging profile by providing constant energy, boosting efficiency and charging reliability under realistic outdoor conditions.

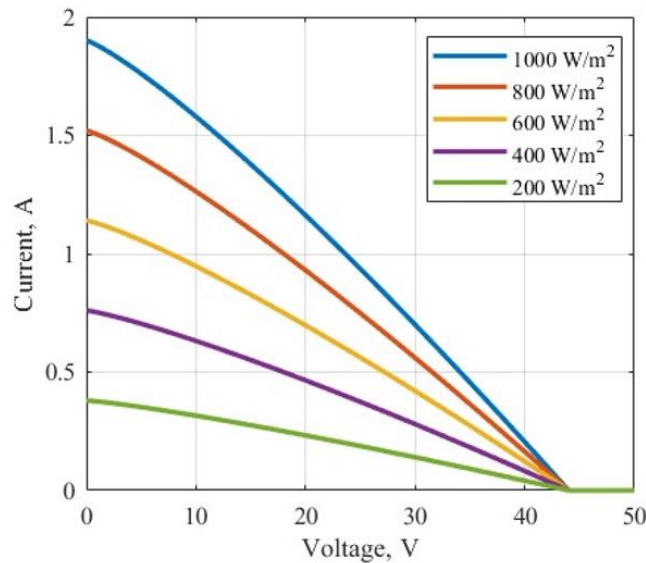


Fig. 19. I-V curves at 25°C.

A 60 W flexible PV module was tested under varying irradiance (200–1000 W/m<sup>2</sup>) and cell temperature (15°C, 25°C, 45°C). The FPGA implemented an MPPT algorithm with 500 Hz sampling, perturbation step  $\Delta V = 0.2$  V, and convergence threshold  $|\Delta P|/P < 0.5\%$ . In the implemented solar interface, the MPPT is carried out using the Perturb-and-Observe (P&O) algorithm, chosen for its simplicity, fast convergence under slowly varying irradiance, and suitability for FPGA-based real-time execution. At STC (1 000 W/m<sup>2</sup>, 25°C),  $V_{mp} = 36.0$  V,  $I_{mp} = 1.67$  A,  $P_{mp} = 60.1$  W, and  $V_{oc} = 44.0$  V. Tracking efficiency remained  $\geq 97.8\%$  across all test points, with convergence times  $< 0.45$  s, validating robust real-time operation. At elevated temperature (45°C),  $V_{mp}$  dropped to 32.8 V with  $P_{mp} = 55.3$  W, while at low temperature (15°C) the maximum output rose to 62.5 W. Dynamic MPPT tests with irradiance step 1000→400 W/m<sup>2</sup> achieved stable convergence within 0.32 s. The stabilized PV contribution ( $\sim 1.6$  A,  $\approx 58$  W) consistently extended the e-bicycle

mileage by  $\sim 15\%$ . The transient response of the PV power under a sudden irradiance drop from 1 000 W/m<sup>2</sup> to 400 W/m<sup>2</sup> is shown in Fig. 17. The FPGA-based MPPT converges smoothly within 0.32 s, maintaining high stability. This demonstrates the fast adaptability and tracking efficiency of the proposed controller.

Figure 18 illustrates P–V characteristics at 25°C for irradiance ranges of 200–1000 W/m<sup>2</sup>. The pronounced peaks indicate accurate maximum power point recognition across conditions. The proposed MPPT reliably aligns with the true  $P_{max}$ , supporting the reported  $\geq 97.8\%$ .

The I–V characteristics for different irradiance ranges are shown in Fig. 19. The observed curves displayed the expected current scaling with irradiance and stable open circuit voltage,  $V_{oc}$ . These results attest to the realistic PV modeling and the system maintains reliable energy harvesting under variable solar input.

A comparative analysis of the mileage and efficiency of the established e-bicycle under four different working

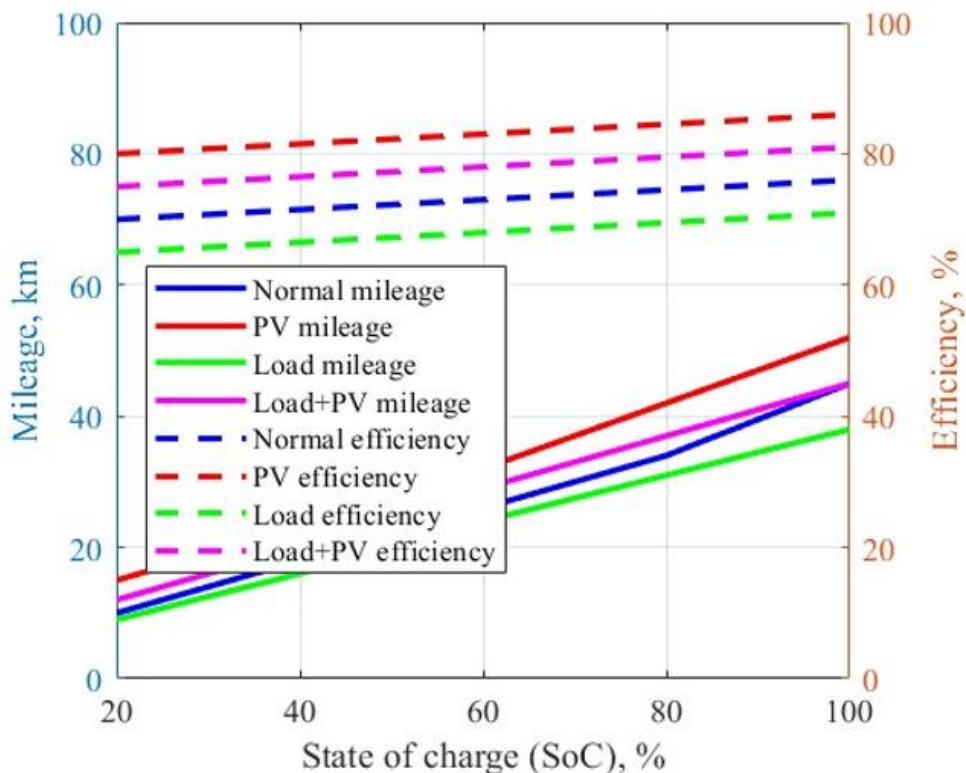


Fig. 20. Mileage and efficiency analysis of e-bicycle.

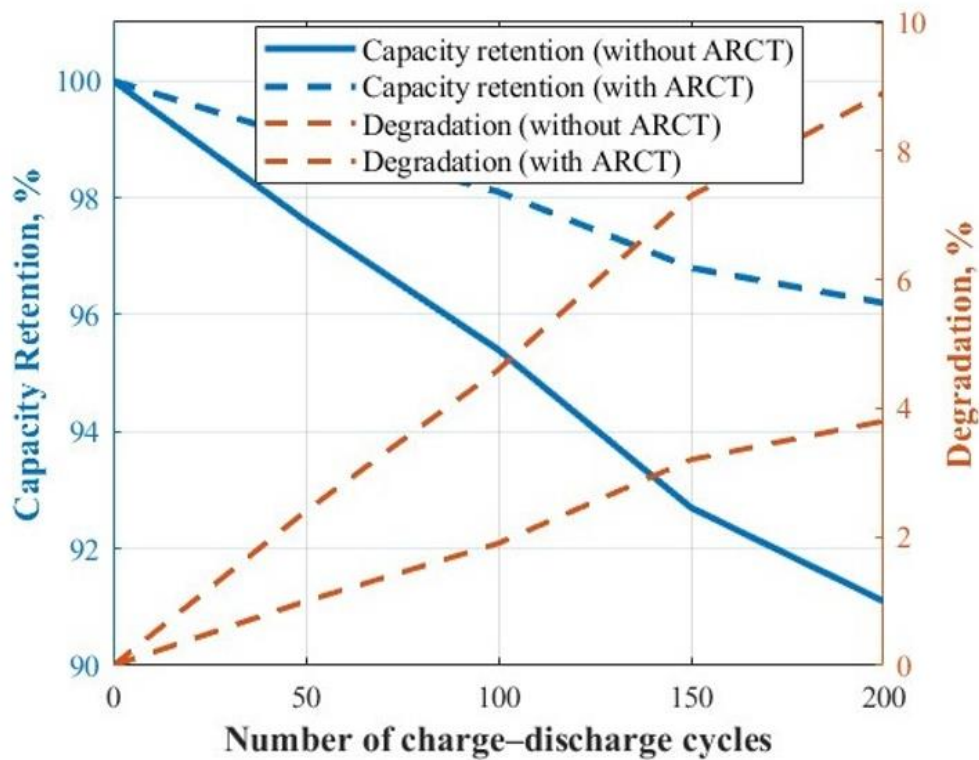


Fig. 21. Battery degradation analysis with and without ARCT control.

conditions, namely, normal operation (battery only), with PV support, loaded with 40 kg, and loaded with PV support, is shown in Fig. 20.

Under normal conditions, the bicycle attained a maximum mileage of 45 km at a 100% SoC. However, the addition of the PV panel increased the mileage to 52 km, authenticating an improvement of nearly 15% in travel range. During the application of 40 kg load, the mileage decreased due to increased power demand, but the presence of PV support partially compensated for this reduction, thus improving overall performance. A similar trend was detected in efficiency, where the PV-assisted modes consistently outperformed the battery-only cases, while the loaded conditions experienced a slight drop due to the increased torque demand. These results suggest that the proposed ARCT and PV integration not only enhances mileage but also withstands higher charging and discharging efficiency, thereby confirming the effectiveness of the designed hybrid e-bicycle system. The design is prone to uncertainties due to sensor tolerance, passive component variations, and environmental variations impacting PV panel output. Small timing delays

during FPGA switching and FFT-based THD measurement also cause modest deviations in measured results. The above uncertainties are likely to cause modest effects on the reported results in mileage estimation and power quality indices but do not offset the measured performance enhancements. Future research should address these issues through the implementation of high-grade sensor calibration, adaptive robust control, and real-time uncertainty modeling to further elevate the level of reliability of the design.

To assess the long-term impact of the proposed ARCT-based charging, a battery degradation analysis was performed over 200 charge-discharge cycles of the e-bicycle's 10-series (10S) NMC lithium-ion pack. Charge-discharge cycling was carried out between 100% and 20% SoC at a discharge current of 3.5 A under controlled ambient conditions of  $27^{\circ}\text{C} \pm 2^{\circ}\text{C}$ . Three individual cells from the pack were additionally monitored to examine stress patterns under conventional charging and ARCT-controlled charging with ripple suppressed below 1.5%. Battery voltage, current, and temperature were recorded using a Keysight digital multimeter, a data logger, and an

TABLE 6. Comparative analysis of the proposed work with the existing works

Parameter	Hysteresis-based control [34]	Average current-mode control [35]	This study
Converter topology	High-gain DC–DC	Integrated 3-phase AC–DC	Super-lift converter (SLC)
Control schema	Modified PI	DSP-based digital PFC control	Adaptive reinforcement-based current tracking (ARCT) using FPGA
Implementation platform	DSP-based controller	Microcontroller	FPGA-based real-time control
Power factor (PF)	0.90	0.998	0.99
Total harmonic distortion (THD)	3.46%	2.87%	2.2%
Ripple in output voltage	~3.5%	~2.87%	< 1.5%
Dynamic response to load variation	Fast but unstable beyond high ripple	Moderate, requires parameter tuning	Fast and adaptive with minimal overshoot
Real-time adaptability	Limited (fixed threshold)	Limited (re-tuning needed)	Self-learning across operating points
Input source	Grid only	Grid only	Grid + flexible solar panel (hybrid source)
Energy backup	None	None	Solar panel backup
Battery charging application	General EV charger	EV on-board charging	E-bicycle (Lightweight mobile application)
Implementation complexity	Simple	Moderate	Higher (but FPGA allows compact execution)

INA219 precision current sensor. The degradation metric was defined as the percentage loss in usable capacity. Figure 21 compares the degradation rates for conventional charging and ARCT-based charging. It is evident that the ARCT-based system kept a more stable charging profile, reducing current ripple and thermal stress on the lithium-ion cells. Subsequently, the cumulative capacity loss after 200 cycles was limited to 3.8%, whereas conventional charging exhibited 8.9% degradation. We attribute this enhancement to the adaptive current tracking and reinforcement-based optimization, which continuously minimized the inductor current error and ensured near-ideal power flow into the battery. The observed difference translated to approximately a 57% reduction in degradation rate, confirming the benefits of the proposed ARCT control in extending battery lifespan.

The comparative analysis in Table 6 shows the improved operation and novelty of the proposed battery charging system in comparison to the two earlier studies.

The comparative analysis highlights that while hysteresis-based control [34] achieved a PF of 0.90 with a

higher THD (3.46%) and ripple (~3.5%), and average current-mode control [35] improved the PF to 0.998 with reduced THD (2.87%) and ripple (~2.87%), both remain limited to the grid-only input and lack adaptability. In contrast, the proposed FPGA-based ARCT control on the SLC attained a near-unity PF (0.99), significantly reduced THD (2.2%), and minimal output ripple (<1.5%) with superior dynamic response and self-learning adaptability. Furthermore, by integrating a flexible solar panel input, the system uniquely provides hybrid energy support and mileage extension for lightweight e-bicycle applications, setting it apart from the conventional grid-only EV charger implementations.

## VII. CONCLUSION

This study presents the design and experimental validation of a hybrid charging and propulsion system for an electric bicycle that integrates a Super-Lift Converter (SLC) controlled by an FPGA-based Adaptive Reinforcement-Based Current Tracking (ARCT) algorithm. The novelty of this study lies in the first reported

application of the ARCT control for an e-bicycle on-board charger. The proposed approach effectively unifies solar and grid-based charging, ensuring uninterrupted operation under stationery and mobility conditions. Without the ARCT, the system had a poor power factor of 0.85 and a total harmonic distortion (THD) of 32.418%. With the ARCT control, the power factor was as high as 0.99 and the input current THD was reduced to 2.211%. The output ripple voltage was maintained within 1.5% peak-to-peak, making the battery safe for charging. The proposed FPGA-based implementation enabled real-time control of the SLC, with the actor-critic algorithm dynamically varying the duty cycle to reduce the current tracking error. Furthermore, the regulated photovoltaic output enabled consistent solar-assisted charging, contributing to a 15% increase in battery-supported mileage. The system successfully charged the battery while providing the grid compliance and ripple-free output, establishing the suitability of ARCT-controlled SLCs for compact and smart electric vehicle charging stations. Although the proposed hybrid charging system delivers optimized performance, certain practical limitations remain. The FPGA experiences computational loads at high sampling rates, while sensor tolerances and temperature-dependent passive component variations can affect learning stability. Moreover, scalability to higher-power electric vehicles will require thermal redesign and enhanced switch ratings, providing clear directions for future work.

#### ACKNOWLEDGMENT

This work was supported by Centre for Sustainable Development, B.S.Abdur Rahman Crescent Institute of Science and Technology, Chennai, India under Crescent Seed Money Project Scheme (Grant No. CSD/SMPS/2023/P1/04).

#### REFERENCES

- [1] T. Myateg, V. Lyubchenko, O. Atamanova, S. Yurkov, E. Mogilenko, "The Influence of electric vehicle charging stations on the quality of power supply to the consumer in Novosibirsk 10/0.4 KV electrical networks," *Energy Syst. Res.*, vol. 6, no. 2, pp. 62–74, 2023. DOI: 10.25729/esr.2023.02.0007.
- [2] L. Stilo, H. Lugo, D. S. Velandia, P. P. Conway, A. A. West, "Personalised controller strategies for next generation intelligent adaptive electric bicycles," *IEEE Trans. Intell. Transp. Syst.*, vol. 22, no. 12, pp. 7814–7825, 2021. DOI: 10.1109/TITS.2020.3009400.
- [3] Y. Li, J. Hu, F. Chen, S. Liu, Z. Yan, Z. He, "A new-variable-coil-structure-based IPT system with load-independent constant output current or voltage for charging electric bicycles," *IEEE Trans. Power Electron.*, vol. 33, no. 10, pp. 8226–8230, 2018. DOI: 10.1109/TPEL.2018.2812716.
- [4] M. Corno, D. Berretta, P. Spagnol, S. M. Savaresi, "Design, control, and validation of a charge-sustaining parallel hybrid bicycle," *IEEE Trans. Control Syst. Technol.*, vol. 24, no. 3, pp. 817–829, 2016. DOI: 10.1109/TCST.2015.2473821.
- [5] G. Suri, S. Onori, "A control-oriented cycle-life model for hybrid electric vehicle lithium-ion batteries," *Energy*, vol. 96, pp. 644–653, 2016. DOI: 10.1016/j.energy.2015.11.075.
- [6] R. C. Hsu, C. T. Liu, D. Y. Chan, "A reinforcement-learning-based assisted power management with QoR provisioning for human-electric hybrid bicycle," *IEEE Trans. Ind. Electron.*, vol. 59, no. 8, pp. 3350–3359, 2012. DOI: 10.1109/TIE.2011.2141092.
- [7] M. Guarisco, F. Gao, D. Paire, "Autonomy and user experience enhancement control of an electrically assisted bicycle with dual-wheel drive," *IEEE Trans. Ind. Appl.*, vol. 53, no. 2, pp. 1476–1484, 2017. DOI: 10.1109/TIA.2016.2617299.
- [8] R. Mai, Y. Chen, Y. Li, Y. Zhang, G. Cao, Z. He, "Inductive power transfer for massive electric bicycles charging based on hybrid topology switching with a single inverter," *IEEE Trans. Power Electron.*, vol. 32, no. 8, pp. 5897–5906, 2017. DOI: 10.1109/TPEL.2017.2654360.
- [9] S. Kuznetsova, V. V. Khanaev, "Alternative possibilities of using electric cars in Siberia," *Energy Syst. Res.*, vol. 5, no. 3, pp. 50–56, 2022. DOI: 10.38028/esr.2022.03.0007.
- [10] Y. Chen, Z. Kou, Y. Zhang, Z. He, R. Mai, G. Cao, "Hybrid topology with configurable charge current and charge voltage output-based WPT charger for massive electric bicycles," *IEEE J. Emerg. Sel. Top. Power Electron.*, vol. 6, no. 3, pp. 1581–1594, 2018. DOI: 10.1109/JESTPE.2017.2782269.
- [11] A. Triviño-Cabrera, J. M. Gonzalez-Gonzalez, J. A. Aguado, "Design and implementation of a cost-effective wireless charger for an electric bicycle," *IEEE Access*, vol. 9, pp. 85277–85288, 2021. DOI: 10.1109/ACCESS.2021.3084802.
- [12] A. A. Patoli, G. Fortino, "FPGA-based system implementation of IEEE 1588 precision time protocol: A review," *IEEE Sens. J.*, vol. 25, no. 11, pp. 18624–18642, 2025. DOI: 10.1109/JSEN.2025.3557277.
- [13] Y. Zhou et al., "Online inductance identification and FPGA-based real-time digital control design for APF," *IEEE Trans. Power Electron.*, vol. 38, no. 2, pp. 1549–1561, 2023. DOI: 10.1109/TPEL.2022.3209893.
- [14] R. N. Tripathi, "Dead-time evaluation with switching frequency for GaN-based non-inverting buck-boost DC–DC converter using FPGA-based high-frequency control," *IEEE J. Emerg. Sel. Top. Power Electron.*, vol. 12, no. 1, pp. 496–504, 2024. DOI: 10.1109/JESTPE.2023.3344458.

- [15] Z. Li, J. Xu, K. Wang, P. Wu, G. Li, "FPGA-based real-time simulation for EV station with multiple high-frequency chargers based on C-EMTP algorithm," *Prot. Control Mod. Power Syst.*, vol. 5, no. 1, 2020. DOI: 10.1186/s41601-020-00171-x.
- [16] F. L. Luo, H. Ye, *Advanced DC/DC converters*. New York, USA: CRC Press, 2003. DOI: 10.1201/9780203492925.
- [17] B. Faridpak, M. Farrokhifar, M. Nasiri, A. Alahyari, N. Sadoogi, "Developing a super-lift Luo-converter with integration of buck converters for electric vehicle applications," *CSEE J. Power Energy Syst.*, vol. 7, no. 4, pp. 811–820, 2020. DOI: <https://doi.org/10.17775/CSEEPES.2020.01880>.
- [18] S. Mahdizadeh, H. Gholizadeh, S. A. Gorji, "A power converter based on the combination of Cuk and positive output super lift Luo converters: Circuit analysis, simulation and experimental validation," *IEEE Access*, vol. 10, pp. 52899–52911, 2022. DOI: 10.1109/ACCESS.2022.3175892.
- [19] F. Ghasemi, M. R. Yazdani, M. Delshad, "Step-up DC-DC switching converter with single switch and multi-outputs based on Luo topology," *IEEE Access*, vol. 10, pp. 16871–16882, 2022. DOI: 10.1109/ACCESS.2022.3150316.
- [20] M. Mahdavi, M. Shahriari-Kahkeshi, N. R. Abjadi, "An adaptive estimator-based sliding mode control scheme for uncertain POESLL converter," *IEEE Trans. Aerosp. Electron. Syst.*, vol. 55, no. 6, pp. 3551–3560, 2019. DOI: 10.1109/TAES.2019.2908272.
- [21] C. Y. Chan, "Adaptive modified current-mode control of a hybrid high voltage gain converter," *IEEE Trans. Circuits Syst. II Express Briefs*, vol. 71, no. 1, pp. 360–364, 2024. DOI: 10.1109/TCSII.2023.3303467.
- [22] X. Jin, J. Qin, S. Member, "Adaptive perturbation rejection control for a class of converter systems with circuit realization," *IEEE Trans. Syst. Man, Cybern. Syst.*, vol. 52, no. 1, pp. 4740–4750, 2022. DOI: 10.1109/TSMC.2021.3103066.
- [23] D. Weber, M. Schenke, O. Wallscheid, "Steady-state error compensation for reinforcement learning-based control of power electronic systems," *IEEE Access*, vol. 11, pp. 76524–76536, 2023. DOI: 10.1109/ACCESS.2023.3297274.
- [24] A. Ahmadian, K. Sedghisigarchi, R. Gadh, "Empowering dynamic active and reactive power control: A deep reinforcement learning controller for three-phase grid-connected electric vehicles," *IEEE Access*, vol. 12, pp. 66068–66084, 2024. DOI: 10.1109/ACCESS.2024.3396449.
- [25] Y. Wan, Q. Xu, T. Dragicevic, "Reinforcement learning-based predictive control for power electronic converters," *IEEE Trans. Ind. Electron.*, vol. 72, no. 5, pp. 5353–5364, 2025. DOI: 10.1109/TIE.2024.3472299.
- [26] D. Jakobeit, M. Schenke, O. Wallscheid, "Meta-reinforcement-learning-based current control of permanent magnet synchronous motor drives for a wide range of power classes," *IEEE Trans. Power Electron.*, vol. 38, no. 7, pp. 8062–8074, 2023. DOI: 10.1109/TPEL.2023.3256424.
- [27] D. Lee, B. Kim, S. Kwon, N. D. Nguyen, M. Kyu Sim, Y. Il Lee, "Reinforcement learning-based control of DC-DC buck converter considering controller time delay," *IEEE Access*, vol. 12, pp. 118442–118452, 2024. DOI: 10.1109/ACCESS.2024.3448535.
- [28] C. Wei, Z. Zhang, W. Qiao, L. Qu, "Reinforcement-learning-based intelligent maximum power point tracking control for wind energy conversion systems," *IEEE Trans. Ind. Electron.*, vol. 62, no. 10, pp. 6360–6370, 2015. DOI: 10.1109/TIE.2015.2420792.
- [29] B. Huangfu, C. Cui, C. Zhang, L. Xu, "Learning-based optimal large-signal stabilization for DC/DC boost converters feeding CPLs via deep reinforcement learning," *IEEE J. Emerg. Sel. Top. Power Electron.*, vol. 11, no. 6, pp. 5592–5601, 2023. DOI: 10.1109/JESTPE.2022.3189078.
- [30] Y. Wan, Q. Xu, T. Dragicevic, "Safety-enhanced self-learning for optimal power converter control," *IEEE Trans. Ind. Electron.*, vol. 71, no. 11, pp. 15229–15234, 2024. DOI: 10.1109/TIE.2024.3363759.
- [31] R. Muduli, D. Jena, T. Moger, "Application of reinforcement learning-based adaptive PID controller for automatic generation control of multi-area power system," *IEEE Trans. Autom. Sci. Eng.*, vol. 22, pp. 1057–1068, 2025. DOI: 10.1109/TASE.2024.3359219.
- [32] G. M. Mustafa, S. I. Gusev, "Active filters for standard-compliant power quality in electrical networks," *Energy Syst. Res.*, vol. 7, no. 1, pp. 51–65, 2024. DOI: 10.25729/esr.2024.01.0006.
- [33] S. S. Sayed, A. M. Massoud, "Review on state-of-the-art unidirectional non-isolated power factor correction converters for short-/long-distance electric vehicles," *IEEE Access*, vol. 10, pp. 11308–11340, 2022. DOI: 10.1109/ACCESS.2022.3146410.
- [34] M. R. Haque, K. M. A. Salam, M. A. Razzak, "A modified PI-controller based high current density DC-DC converter for EV charging applications," *IEEE Access*, vol. 11, pp. 27246–27266, 2023. DOI: 10.1109/ACCESS.2023.3258181.
- [35] J. Liu, C. S. Wong, Z. Li, X. Jiang, K. H. Loo, "An integrated three-phase AC-DC wireless-power-transfer converter with active power factor correction using three transmitter coils," *IEEE Trans. Power Electron.*, vol. 38, no. 6, pp. 7821–7835, 2023. DOI: 10.1109/TPEL.2023.3238877.
- [36] X. Huang, X. Ruan, L. Zhang, F. Liu, "Second harmonic current reduction schemes for DC-DC converter in two-stage PFC converters," *IEEE Trans. Power Electron.*, vol. 37, no. 1, pp. 332–343, 2022. DOI: 10.1109/TPEL.2021.3099170.



**Shajini G Inba Kani** is currently a Research Scholar at B.S. Abdur Rahman Crescent Institute of Science and Technology, Chennai, and serves as an Assistant Professor with the Department of Electrical and Electronics Engineering at Dhaanish Ahmed College of Engineering, Chennai. She obtained her Bachelor of Engineering (B.E.) degree in 2008 and Master of Engineering (M.E.) degree in 2011 from Anna University. With a strong academic background and over a decade of teaching experience, her research interests focus on power electronics and electric vehicle technology, particularly in the areas of energy management and converter design for sustainable mobility solutions.



**P. Elangovan** is currently an Assistant Professor with the Department of Electrical and Electronics Engineering at B.S. Abdur Rahman Crescent Institute of Science and Technology, Chennai. He received all his academic degrees from Anna University, including the B.E. in Electrical and Electronics Engineering (2007), the M.E. in Power Electronics and Drives (2011), and the Ph.D. in Electrical Engineering (2017). With over 15 years of academic and research experience, he specializes in power electronics, electric vehicles, and embedded systems. He has guided several postgraduate and doctoral scholars, with research interests focusing on advanced DC-DC converter topologies, high-gain converters, predictive control strategies for power factor correction, and sustainable energy management systems for electric mobility. Dr. Elangovan has published extensively in leading international journals and conferences and is an active member of IEEE. He also plays a key role in organizing technical events, mentoring students, and facilitating industry-academia collaborations. His contributions extend to curriculum development, consultancy, and innovation in engineering education. Through his continued commitment to research excellence and academic leadership, he is a major contributor to the advancement of power electronics and sustainable mobility technologies in India.